

X-ray absorption fine structure for single crystals

Christopher T. Chantler,^{a*} Chanh Q. Tran^b and Zwi Barnea^a^aSchool of Physics, University of Melbourne, Australia, and ^bDepartment of Physics, La Trobe University, Australia. Correspondence e-mail: chantler@unimelb.edu.au

X-ray absorption fine structure measurements are a prime tool at synchrotrons around the world, accounting for over 30% of all synchrotron research. They are incisive tools for elucidating local structure, ionization state and coordination geometry. However, in general, it has not been possible to apply them to perfect or near-perfect crystals, and their dominant application is to micro-samples, powders, metals and solutions. The reasons for this are given, and an experimental technique to yield high-precision data for good crystals is developed. This widens the applicability of the technique dramatically, and permits standards and calibration samples to be used and transferred for new types of measurement. It is shown that this is particularly appropriate for discrete measurements of absorption, X-ray absorption fine structure and X-ray absorption near-edge spectroscopy, and in cases of strong oscillations.

© 2010 International Union of Crystallography
Printed in Singapore – all rights reserved

1. Introduction

A standard X-ray absorption fine structure (XAFS) measurement will measure the transmission of a sample as a function of energy above a particular absorption edge. The sudden jump in absorption coefficient at the edge indicates that enough energy is imparted by the incoming photon to release the bound photoelectron, in the inverse photo-effect. In the region extending some eV to keV above the edge, strong oscillations are often seen. These oscillations reflect the interference effect due to the photoelectron wave scattering from the surrounding electron density and interfering with the original outgoing wave. A schematic diagram illustrating the process is given in Fig. 1. This fine structure can then be inverted (or Fourier transformed) to display the radial electron density at some distance from the atom containing the absorption edge that emitted the photoelectron (Sayers *et al.*, 1971).

Hence, the structure observed is used to characterize the solid-state electron wavefunction (Rehr & Albers, 2000), and thereby can be fitted to a number of theoretical models (Newville, 2001; Joly, 2001; Bourke *et al.*, 2007) to obtain oxidation states of species (Ryser *et al.*, 2005; Takahashi *et al.*, 2002), nearest-neighbour distances (Hwang *et al.*, 2000), coordination numbers (Matteo *et al.*, 2005; Ravel *et al.*, 2006) and thermal parameters (Fornasini *et al.*, 2004) and to confirm structural evaluations (Gawelda *et al.*, 2006). For complex species such as organometallics (Glover *et al.*, 2007) or biologically active systems (Loll *et al.*, 2005; Haumann *et al.*, 2005) this technique can very usefully characterize the active centres of bioactive or chemically active molecules.

The XAFS technique has found its dominant application to micro-samples in the environmental and earth sciences (Hedman & Pianetta, 2007*a*), biological and medical solutions (Hedman & Pianetta, 2007*b*), thin films (Wei *et al.*, 2000), powders (Artioli *et al.*, 2006), solid solutions (Greaves & Sen,

2007), melts (Okamoto *et al.*, 2002), and metals and alloys (Felderhoff *et al.*, 2004). However, in general, it has not been possible to apply XAFS to perfect or near-perfect crystals (Glover & Chantler, 2007; Riggs-Gelasco *et al.*, 1995; Crozier, 1997). We discuss one precondition for obtaining good XAFS spectra – that coherent scattering of the incident X-ray is negligible compared to the photo-absorption amplitude – and explain the consequences of this condition. In particular, this condition has limited the application of the technique to the above types of samples and has limited the potential for defining transfer and calibration standards. We discuss how this significant limitation can be addressed to enable useful and high-precision experiments on high-quality crystals and crystallites of intermediate perfection.

2. The problem: discontinuities and singularities in experimental data sets

The typical XAFS spectrum as illustrated in Fig. 2 for metallic tin has sharp features on the absorption edge, progressing to

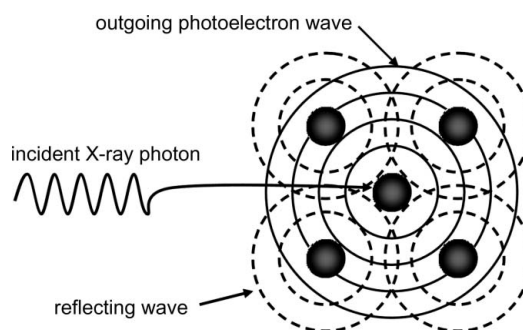


Figure 1

Illustration of the interference of the outgoing and returning photoelectron waves for a simple geometry, leading to X-ray absorption fine structure.

smoother and continuous waves further above the edge, until after some keV the interference signal is lost and a smooth background curve is reached. Depending upon the quality of the data set, detector and counting noise will often dominate in this region, defining a natural cut-off for standard XAFS analysis. The near-edge region (X-ray absorption near-edge structure) or the intermediate region (central XAFS) may be analysed for coordination, nearest neighbours, oxidation state and structure. In principle, smooth curves with a precision of better than 1%, and occasionally 0.1%, can be obtained across the full range of the study.

However, for high-quality crystals this usually does not work, and large discontinuities of 10% or more spike the data set (Fig. 3). Often this (long-range interference effect) invalidates the study, and the data are discarded. In part, this is because the theory of the oscillations requires a smooth function with a well defined periodicity, and singularities tend to invalidate any fitting routine.

An example of such a situation has been represented recently (Ruffoni, Pettifer, Pascarelli & Mathon, 2007) by the developers of differential XAFS (DAXS) (Pettifer *et al.*, 2005; Ruffoni, Pettifer, Pascarelli, Trapananti *et al.*, 2007; Ruffoni & Pettifer, 2006). In that paper, the standard XAFS technique is shown to fail simply by replacing a polycrystalline material (SrF_2) with a corresponding single-crystal sample. While the single crystal is a better defined object and makes a preferred standard for research, as a cross-calibration between beam-lines or in the presence of varying tuning conditions, the additional structure introduced destroys our ability to interpret the measurements.

The above authors use their differential technique to define a useful source of investigation, namely a differential X-ray diffraction signal superimposed upon the XAFS. The magnitude and widths of the spikes involved are similar to those of the 'real' XAFS oscillations, which can sometimes explain the

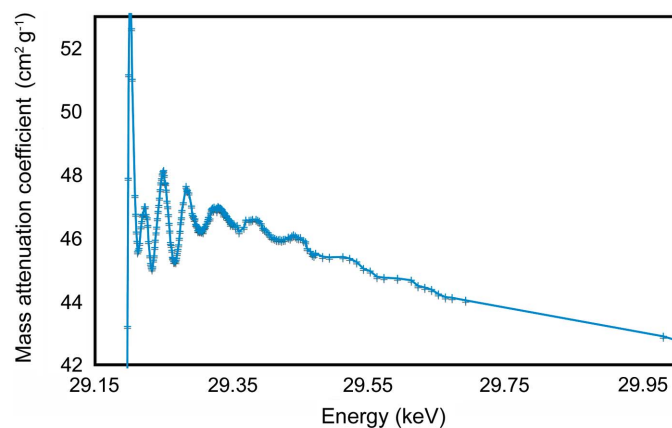


Figure 2

Detail of the measured absolute mass in the region of the XAFS, with error bars typically 0.1–0.2% representing the accuracy. Usually these standard errors are dominated by the contribution from limitations of precision (from statistics), or limitations of the materials characterization (thickness, density, profile and purity) or the experimental systematics (bandpass, harmonics, detector noise and linearity). The absorbers in this experiment spanned a wide range of attenuations at each measured energy, allowing attenuation-dependent systematic errors to be detected.

difficulty of analysing a sample of unknown perfection. Of course, most samples are of unknown perfection, but fortunately many are randomly oriented microcrystallites.

3. Measuring mass attenuation coefficients

Accurate measurements of (μ/ρ) , the mass attenuation coefficient, find application in a wide range of fields including medical imaging (Lee *et al.*, 1991; Kinahan *et al.*, 1998), radiation shielding (Ipe & Fasso, 1994) and chemical structure determination (Hasnain *et al.*, 1999). The X-ray mass attenuation coefficient of a sample is measured in transmission geometry using the Beer–Lambert equation:

$$\exp[-(\mu/\rho)(\rho t)] = I/I_0. \quad (1)$$

Here, I_0 is proportional to the number of photons striking the sample and I is proportional to the number of photons transmitted through that sample. I_0 and I are measured in an experiment, then equation (1) is used to determine $(\mu/\rho)(\rho t)$, the relative mass attenuation coefficient. The final step in determining (μ/ρ) is to determine (ρt) , the integrated column density of the sample along the path of the X-ray beam. The integrated column density is defined as follows:

$$(\rho t) = \int_P \rho(\mathbf{x}) dt, \quad (2)$$

where P is the path of the X-ray beam and $\rho(\mathbf{x})$ is the local density of the sample at the point \mathbf{x} . Since the X-ray beam has a finite size, different parts of the beam take different parallel paths through the sample. For a rough sample, each of these paths will have a different (ρt) value. Using a value of (ρt) averaged across the beam area is not sufficient to determine

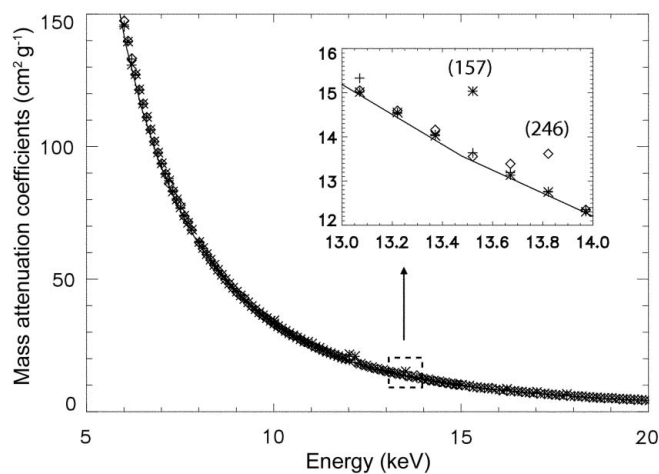


Figure 3

Mass attenuation coefficients of silicon as a function of energy. The three symbols indicate the experimental results obtained with samples of slightly different orientations with respect to the incident beam and the continuous line is the calculated theoretical mass attenuation coefficient from Tran, Chantler, Barnea *et al.* (2003). The magnified section shows the effect of diffraction by the (157) and (246) planes occurring for one of the samples used. Although the discontinuities look 'small' on this plot, these spikes invalidate the Fourier transform and generate spurious apparent information content.

(μ/ρ) correctly. This effect causes a potentially large systematic error in measurements of (μ/ρ) made of rough samples. Indeed, the signature of this systematic error can be used to define the magnitude of the roughness (de Jonge *et al.*, 2005a; Glover *et al.*, 2009).

In order to obtain a highly accurate determination of (μ/ρ) , free from dominant systematic errors, one must take a careful approach. The X-ray extended range technique (XERT) (Chantler, Tran, Paterson *et al.*, 2001; Tran, Chantler & Barnea, 2003; Chantler, Tran, Barnea *et al.*, 2001) has allowed for the correction of a wide range of systematic errors and produces results of extremely high accuracy.

A typical experimental set-up used by the XERT is shown in Fig. 4. The X-ray beam from a synchrotron is passed through a de-tuned double-crystal monochromator in order to select the required energy of the X-ray beam. The beam energy is accurately determined using a powder diffractometer (Rae *et al.*, 2006; Barnea *et al.*, 1992) and powder sample standards (Parrish *et al.*, 1999; Rasberry *et al.*, 1989).

The XERT has been able to correct for many systematic errors, including scattering, fluorescence, harmonics (Tran, Barnea *et al.*, 2003; de Jonge *et al.*, 2004a), and the attenuation of the ion chambers and air path. The XERT uses the full-foil mapping technique (de Jonge *et al.*, 2004b) to determine (ρt) (Tran *et al.*, 2004). This process of determining (ρt) is usually performed for two or three samples, with the remaining unknown (ρt) values determined using a fitting procedure. Using these methods the XERT has been able to produce the most accurate determination of (μ/ρ) of any substance or energy range so far published (de Jonge *et al.*, 2005b).

4. How coherent scattering affects the mass attenuation coefficient

On occasion, single-crystal samples are used to obtain XAFS and absorption spectra for comparison with spectra obtained with films or solutions, or in order to study the spectra as a function of crystal orientation (Ruffoni, Pettifer, Pascarelli & Mathon, 2007; Ruffoni, Pettifer, Pascarelli, Trapananti *et al.*, 2007; Ruffoni & Pettifer, 2006; Pettifer *et al.*, 2005). When the absorption of X-rays is measured using single-crystal absorbers, the otherwise smooth trend of the absorption is periodically interrupted by sharp increases in the value of the mass

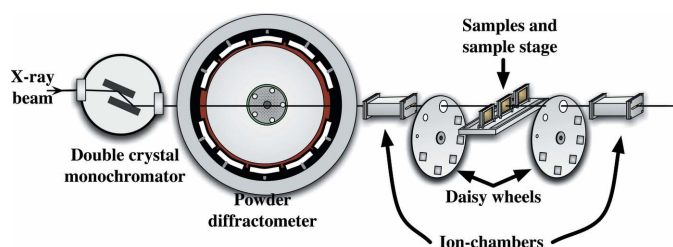


Figure 4 A typical set-up used during an experiment utilizing the XERT. The monochromated collimated X-ray beam is normalized by matched ion chambers before and after the sample; the energy is measured explicitly by, for example, a powder diffractometer; harmonic contamination or broad scattering contributions are measured by absorbers and apertures mounted upon daisy wheels.

absorption coefficient (Fig. 3). Investigation of these sharp absorption jumps has shown that they are due to the occurrence of diffraction whenever the orientation of the single crystal and the X-ray energy result in the Bragg–Laue condition being satisfied (Tran, Chantler, Barnea *et al.*, 2003). When this occurs, the diffracted beam redirects some of the incident-beam intensity, thereby decreasing the intensity of the X-rays reaching the counter; this results in the apparent increase of the absorption (Fig. 5). The occurrence of these apparent absorption increases in regions where the absorption changes smoothly with energy is clearly marked and easily recognized. In the extended XAFS region the presence of absorption structure makes it much more difficult to recognize such absorption increases.

5. Laue–Bragg scattering

Fig. 6 shows the percentage differences in the measured mass attenuation coefficients for five samples, three of which were used at each energy, compared with their average (zero line). Below 5.6 keV we observed divergences between the three measurements due to the effect of the harmonic contamination in the incident beam as discussed in §4. Above 5.6 keV the three measurements are consistent within 0.5%. However, we observe some local discontinuous increases (at the level of 1–8%) in the mass attenuation coefficient measured with one sample compared to the other two consistent measurements.

This is explained by Laue–Bragg diffraction occurring in the crystals. This diffraction extracts more photons out of the beam, resulting in significantly higher measured attenuation. The three single-crystal specimens do not have the same orientations relative to the incident beam and therefore do not exhibit Laue–Bragg diffraction at the same energies.

In many previous attenuation measurements using crystalline samples, it has been assumed that Laue–Bragg scattering did not occur during the experiments. It has also been suggested that by highly collimating the incident beam

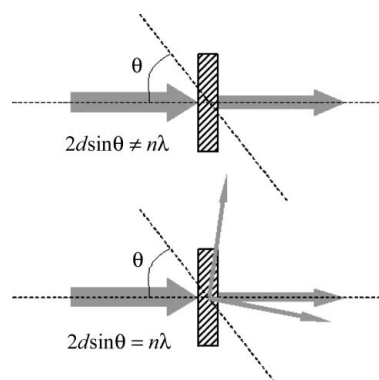


Figure 5 A schematic of absorption with a Bragg peak and without. The lower diagram shows that, when the Bragg or Laue condition is satisfied, the intensity diffracted is of course also lost to the attenuated transmitted beam, implying a higher apparent absorption coefficient. Hence, this appears as a sudden, sharp spike in the absorption, confusing standard analysis.

Table 1

Determination of the diffraction planes responsible for the observed jump in the measured mass attenuation coefficient.

Column 3 shows the diffraction plane yielding the peak; column 4 shows the fitted direction of the incident X-ray beam relative to the crystal planes; and column 5 ($\Delta I/I$ in %) shows the magnitude of the observed intensity deviation due to the Laue–Bragg diffraction condition being nearly satisfied.

Sample (mm)	E_{cal} (keV)	Bragg (hkl)	[111] Orientation [hkl]	$\Delta I/I$ (%)
0.05	7.5134	(1 $\bar{3}\bar{3}$)	[1.000 1.000 1.000]	1.39
0.25	13.8220	($\bar{2}$ 46)	[1.000 1.000 1.000]	6.46
0.25	14.2723	($\bar{4}$ 88)	[1.000 1.000 1.000]	1.39
0.25	15.8256	($\bar{8}$ 00)	[1.000 1.000 1.000]	4.27
0.25	18.0274	($\bar{5}$ 911)	[1.000 1.000 1.000]	1.25
0.25	18.2259	($\bar{1}$ 19)	[1.000 1.000 1.000]	2.74
0.4	9.7164	($\bar{1}$ 35)	[1.002 1.001 1.000]	1.57
0.4	10.0172	(1 $\bar{3}$ 5)	[1.002 1.001 1.000]	3.49
0.4	10.9203	(357)	[1.002 1.001 1.000]	1.99
0.4	11.0202	($\bar{3}$ 57)	[1.002 1.001 1.000]	2.42
0.4	12.0209	($\bar{2}$ 24)	[1.002 1.001 1.000]	9.19
0.4	12.1711	(377)	[1.002 1.001 1.000]	11.52
0.4	13.5215	(1 $\bar{5}$ 7)	[1.002 1.001 1.000]	10.32
0.4	15.2264	(179)	[1.002 1.001 1.000]	1.48
0.4	16.2252	($\bar{1}$ 59)	[1.002 1.001 1.000]	5.26
0.4	17.0274	(335)	[1.002 1.001 1.000]	6.77
0.4	17.2278	(1311)	[1.002 1.001 1.000]	1.88
0.4	17.8270	(115)	[1.002 1.001 1.000]	9.11
0.5a	10.8203	(466)	[1.002 1.000 1.000]	2.31
0.5a	13.0706	($\bar{1}$ 77)	[1.002 1.000 1.000]	1.98
0.5b	19.0264	($\bar{1}$ 99)	[1.011 1.004 0.999]	2.14
0.5b	20.0281	(13 $\bar{1}$ 1)	[1.011 1.004 0.999]	4.09

(Creagh & Hubbell, 1987), Laue–Bragg diffraction can be avoided or minimized.

We confirmed this effect by using the known lattice parameter and orientation of our single-crystal absorbers to calculate the energies at which the Bragg condition is satisfied. This enabled us to account for each sudden absorption increase and confirmed our explanation of the structural

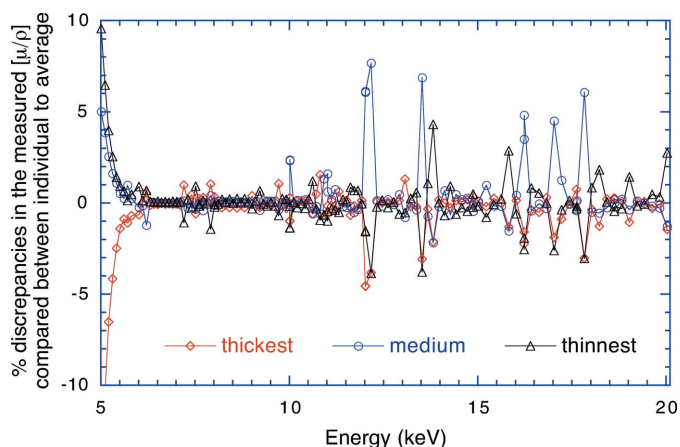


Figure 6

Per cent discrepancy between the measurements of (μ/ρ) using three samples compared with the average as a function of energy. Below 5.6 keV, the divergence shows the effect of harmonic contamination before applying the correction procedure described by Tran, Chantler, Barnea *et al.* (2003). Above 5.6 keV, the discrepancies are less than 0.5% in most cases. The discontinuous increase in the results for one specimen indicates that, simultaneously with absorption, Laue–Bragg diffraction is occurring in that specimen.

Table 2

Deviation $\delta\theta$ between the nominal directions of the incident beam onto the samples ([111]) and the directions corresponding to minimal differences between the X-ray energies and the energies satisfying the Laue–Bragg conditions.

Column 1 gives the sample thicknesses, columns 2–4 show the fitted directions of the incident beams, and column 5 shows the deviations (in $^\circ$) between the fitted direction and the nominal direction.

Sample thickness (mm)	[hkl] [111]	$\delta\theta$ ($^\circ$)
0.05	[1.000 1.000 1.000]	0.00
0.25	[1.000 1.000 1.000]	0.00
0.4	[1.002 1.001 1.000]	0.05
0.5a	[1.002 1.000 1.000]	0.05
0.5b	[1.011 1.004 0.999]	0.28

variation between samples. We conducted simple θ – 2θ diffraction measurements using our local source to determine the orientations of all crystals used in the attenuation measurements. The results showed that all of the crystals have an approximate [111] orientation.

Computer programs were developed to confirm that the observed discrepancies are due to Laue–Bragg diffraction by checking if there are diffraction planes with indices [hkl] that meet the Laue–Bragg condition at which the anomalies were observed. Given that the incident beam was close to the normal [111] directions of the wafers, the angle θ_{norm} between the incident beam and the normal direction of an (hkl) plane is calculated by

$$\theta_{\text{norm}} = \arccos \left\{ \frac{h_0 \times h + k_0 \times k + l_0 \times l}{[(h_0^2 + k_0^2 + l_0^2)(h^2 + k^2 + l^2)]^{1/2}} \right\} \quad (3)$$

where h_0, k_0, l_0 are 1, 1, 1 and the calculated θ_{norm} is in the range $0 \leq \theta_{\text{norm}} \leq \pi$. The incident angle θ of the beam relative to the (hkl) planes is then $\theta = (\theta_{\text{norm}} - \pi/2)$ if $\theta_{\text{norm}} > \pi/2$, or $\theta = (\pi/2 - \theta_{\text{norm}})$ if $\theta_{\text{norm}} < \pi/2$.

Discrepancies between calibrated energies and the best-fit Laue–Bragg energies are partly due to the direction of the incident beam being slightly different from the [111] directions of the crystals. The nominal direction of the incident beam ([111]), or equivalently the nominal orientation of the crystals relative to the incident beam, was therefore varied by small amounts (change in the Miller indices by ± 0.2 in 0.001 steps). The [hkl] directions that give the minimum sum of the squared discrepancies between the calibrated X-ray energies and the Laue–Bragg energies for each sample are listed in Table 1. This experimental result confirmed the conclusions of the model and, for example, confirmed the primary cut of the crystals compared to *e.g.* a possible [220] orientation (Tran, 2002).

This small variation of the direction of the incident beam is consistent with experimental positioning and improves considerably the consistency between the Laue–Bragg energies and the calibrated energies as listed in Table 1. The corresponding angular discrepancies between the best-fit and nominal directions of the incident beam are listed in Table 2. Incidentally, these comparisons confirm the approximately

[111] orientation of these samples, which was however tested by independent measurement.

6. Discussion

Any attempt to correct for the diffraction effect requires, in addition to knowledge of the energy at which it occurs, a calculation of the magnitude of the excursion, and the width of the profile in energy and angular space. This in turn requires accurate knowledge of the atomic form factors, of the structure factors including the Debye–Waller factors, of the state of perfection of the crystal and its precise orientation, and of the value of the absorption coefficient of the diffracting crystal. Correction for this effect is therefore not a simple matter.

In the X-ray extended range technique we measure the absorption as a function of energy using a number of single crystals of different orientations and thicknesses, and having accounted for the diffraction effect we can pool the data unaffected by such resonances. In general, the XAFS or absorption spectra can be measured using a number of single crystals of different orientations. This will result in spectra with diffraction effects occurring at different energies as shown in Fig. 6. The strongly affected points in energy and orientation where these effects occur can then be discarded and, after suitable normalization of the spectra, one can obtain a Bragg-peak-free attenuation coefficient for absorption or XAFS analysis by combining the diffraction-free sections (Tran, Chantler, Barnea *et al.*, 2003).

One can avoid the diffraction effect using a single-crystal sample by deliberately misorienting the sample. Even a small change of orientation of the sample relative to the incident X-ray beam results in an energy shift of the diffraction-caused excursion. This can be used to map a particular Bragg profile or resonance. Of course, the patterns obtained with a misoriented sample correspond to slightly different effective sample thicknesses. These can then be combined to yield a single pattern free of diffraction effects. By tilting the specimens to search for an angular position that in the neighbourhood of the measured attenuation is smooth (Baltazar-Rodrigues & Cusatis, 2001), such Laue–Bragg diffraction can be avoided. This is possible for experiments using a single sample at a few energies, but is extremely inefficient for extended measurements over large ranges, where data for several single crystals should be obtained.

It is interesting to consider whether such absorption excursions can also be observed when the sample is polycrystalline. Polycrystalline samples offer even more opportunities for the Bragg condition to be satisfied, especially when the X-ray beam illuminates a number of single-crystal regions or crystallites. However, the magnitude of the effect, proportional as it is to the volume of the single crystallites, is then much smaller and the effect thus more difficult to observe. Even if, under these conditions, the individual absorption excursions lack prominence, they will contribute to a general background which is very difficult to separate from the total absorption. Hence, it is possible that the most accurate absorption measurements may in fact be obtained with single-

crystal specimens in which the diffraction effect is prominent and can be both observed and avoided. The most likely opportunity to observe the diffraction effect in polycrystalline materials may be furnished by carefully prepared metallic foils with relatively large single-crystal grains.

This work was supported by the Australian Synchrotron Research Program which is funded by the Commonwealth of Australia under the Major National Research Facilities Program and by a number of grants of the Australia Research Council. Use of the Advanced Photon Source was supported by the US Department of Energy, Basic Energy Sciences, the Office of Energy Research, under contract No. W-31-109-Eng-38. We are grateful for the assistance of the synchrotron staff at beamline 20B of the Photon Factory in Tsukuba, Japan.

References

- Artioli, G., Dapiaggi, M., Fornasini, P., Sanson, A., Rocca, F. & Merli, M. (2006). *J. Phys. Chem. Solids*, **9**, 1918–1922.
- Baltazar-Rodrigues, J. & Cusatis, C. (2001). *Nucl. Instrum. Methods Phys. Res. Sect. B*, **179**, 325–333.
- Barnea, Z., Creagh, D. C., Davis, T. J., Garrett, R. F., Janky, S., Stevenson, A. W. & Wilkins, S. W. (1992). *Rev. Sci. Instrum.* **63**, 1069–1072.
- Bourke, J., Chantler, C. T. & Witte, C. (2007). *Phys. Lett. A*, **360**, 702–706.
- Chantler, C. T., Tran, C. Q., Barnea, Z., Paterson, D., Cookson, D. J. & Baliac, D. X. (2001). *Phys. Rev. A*, **64**, 062506.
- Chantler, C. T., Tran, C. Q., Paterson, D., Cookson, D. & Barnea, Z. (2001). *Phys. Lett. A*, **286**, 338–346.
- Creagh, D. C. & Hubbell, J. H. (1987). *Acta Cryst.* **A43**, 102–112.
- Crozier, E. D. (1997). *Nucl. Instrum. Methods Phys. Res. Sect. B*, **133**, 134–144.
- Di Matteo, S., Joly, Y. & Natoli, C. R. (2005). *Phys. Rev. B*, **72**, 144406.
- Felderhoff, M., Klementiev, K., Grunert, W., Spliethoff, B., Tesche, B., von Colbe, B. J. M., Bogdanovic, B., Hartel, M., Pommerin, A., Schuth, F. & Weidenthaler, C. (2004). *Phys. Chem. Chem. Phys.* **17**, 4369–4374.
- Fornasini, P., Beccara, S. A., Dalba, G., Grisenti, R., Sanson, A., Vaccari, M. & Rocca, F. (2004). *Phys. Rev. B*, **70**, 174301.
- Gawelda, W., Johnson, M., de Groot, F. M. F., Abela, R., Bressler, C. & Chergui, M. (2006). *J. Am. Chem. Soc.* **128**, 5001–5009.
- Glover, J. L. & Chantler, C. T. (2007). *Meas. Sci. Technol.* **18**, 2916–2920.
- Glover, J. L., Chantler, C. T. & de Jonge, M. D. (2009). *Phys. Lett. A*, **373**, 1177–1180.
- Glover, J. L., Chantler, C. T., Soldatov, A. V., Smolentsev, G. & Feiters, M. C. (2007). *AIP Conf. Proc.* **882**, 625–627.
- Greaves, G. N. & Sen, S. (2007). *Adv. Phys.* **56**, 1–166.
- Hasnain, S. S., Helliwell, J. R. & Kamitsubo, H. (1999). *J. Synchrotron Rad.* **6**, 121–122.
- Haumann, M., Muller, C., Liebisch, P., Barra, M., Grabolle, M. & Dau, H. (2005). *Biochemistry*, **44**, 1894–1908.
- Hedman, B. & Pianetta, P. (2007a). Editors. *AIP Conf. Proc.* **882**, 173–300.
- Hedman, B. & Pianetta, P. (2007b). Editors. *AIP Conf. Proc.* **882**, 301–360.
- Hwang, J., Krebs, C., Huynh, B.-H., Edmondson, D. E., Theil, E. C. & Penner-Hahn, J. E. (2000). *Science*, **287**, 122–125.
- Ipe, N. E. & Fasso, A. (1994). *Nucl. Instrum. Methods Phys. Res. Sect. A*, **351**, 534–544.
- Joly, Y. (2001). *Phys. Rev. B*, **63**, 125120.
- Jonge, M. D. de, Barnea, Z., Tran, C. Q. & Chantler, C. T. (2004a). *Phys. Rev. A*, **69**, 022717.

- Jonge, M. D. de, Barnea, Z., Tran, C. Q. & Chantler, C. T. (2004*b*). *Meas. Sci. Technol.* **15**, 1811–1822. <http://adsabs.harvard.edu/abs/2004MeScT.15.1811D>, provided by the Smithsonian/NASA Astrophysics Data System.
- Jonge, M. D. de, Tran, C. Q., Chantler, C. T., Barnea, Z., Dhal, B. B., Cookson, D. J., Lee, W.-K. & Mashayekhi, A. (2005*a*). *Phys. Rev. A*, **71**, 032702.
- Jonge, M. D. de, Tran, C. Q., Chantler, C. T., Barnea, Z., Dhal, B. B., Cookson, D. J., Lee, W. K. & Mashayekhi, A. (2005*b*). *Phys. Rev. A*, **71**, 032703.
- Kinahan, P. E., Townsend, D. W., Beyer, T. & Sashin, D. (1998). *Med. Phys.* **25**, 2046–2053.
- Lee, M. J., Hahn, P. F., Papanicolaou, N., Egglin, T. K., Saini, S., Mueller, P. R. & Simeone, J. F. (1991). *Radiology*, **179**, 415–418.
- Loll, B., Kern, J., Saenger, W., Zouni, A. & Biesiadka, J. (2005). *Nature (London)*, **438**, 1040–1044.
- Newville, M. (2001). *J. Synchrotron Rad.* **8**, 322–324.
- Okamoto, Y., Shiwaku, H., Yaita, T., Narita, H. & Tanida, H. (2002). *J. Mol. Struct.* **641**, 71–76.
- Parrish, W., Wilson, A. J. C. & Langford, J. I. (1999). *International Tables for Crystallography*, Vol. C, pp. 421–431. Dordrecht: Kluwer Academic Publishers.
- Pettifer, R. F., Mathon, O., Pascarelli, S., Cooke, M. D. & Gibbs, M. R. J. (2005). *Nature (London)*, **435**, 78–81.
- Rae, N. A., Chantler, C. T., Tran, C. Q. & Barnea, Z. (2006). *Rad. Phys. Chem.* **75**, 2063–2066.
- Rasberry, S., Hubbard, C., Zhang, Y. & McKenzie, R. (1989). *Standard Reference Material Certificates, Standard Reference Material 660*, NIST, Gaithersburg, MD, USA.
- Ravel, B., Kim, Y.-I., Woodward, P. & Fang, C. (2006). *Phys. Rev. B*, **73**, 184121.
- Rehr, J. J. & Albers, R. C. (2000). *Rev. Mod. Phys.* **72**, 621–654.
- Riggs-Gelasco, P. J., Stemmler, T. L. & Penner-Hahn, J. E. (1995). *Coord. Chem. Rev.* **144**, 245–286.
- Ruffoni, M. P. & Pettifer, R. F. (2006). *J. Synchrotron Rad.* **13**, 489–493.
- Ruffoni, M. P., Pettifer, R. F., Pascarelli, S. & Mathon, O. (2007). *J. Synchrotron Rad.* **14**, 169–172.
- Ruffoni, M. P., Pettifer, R. F., Pascarelli, S., Trapananti, A. & Mathon, O. (2007). *J. Synchrotron Rad.* **14**, 421–425.
- Ryser, A. L., Strawn, D. G., Marcus, M. A., Johnson-Maynard, J. L., Gunter, M. E. & Moller, G. (2005). *Geochem. Trans.* **6**, 1–11.
- Sayers, D. E., Stern, E. A. & Lytle, F. W. (1971). *Phys. Rev. Lett.* **27**, 1204–1207.
- Takahashi, Y., Usui, A., Okumura, K., Uruga, T., Nomura, M., Murakami, M. & Shimizu, H. (2002). *Chem. Lett.* **3**, 366–367.
- Tran, C. Q. (2002). PhD thesis, University of Melbourne, Australia.
- Tran, C. Q., Barnea, Z., de Jonge, M. D., Dhal, B. B., Paterson, D., Cookson, D. J. & Chantler, C. T. (2003). *X-ray Spectrom.* **32**, 69–74.
- Tran, C. Q., Chantler, C. T. & Barnea, Z. (2003). *Phys. Rev. Lett.* **90**, 257401.
- Tran, C. Q., Chantler, C. T., Barnea, Z. & de Jonge, M. D. (2004). *Rev. Sci. Instrum.* **75**, 2943–2949. <http://adsabs.harvard.edu/abs/2004RSci...75.2943T>, provided by the Smithsonian/NASA Astrophysics Data System.
- Tran, C. Q., Chantler, C. T., Barnea, Z., Paterson, D. & Cookson, D. J. (2003). *Phys. Rev. A*, **67**, 42716.
- Wei, S. Q., Oyanagi, H., Sakamoto, K., Takeda, Y. & Pearsall, T. P. (2000). *Phys. Rev. B*, **62**, 1883.